

Optical and strain stabilization of point defects in silicon carbide

Cite as: Appl. Phys. Lett. **120**, 184001 (2022); doi: [10.1063/5.0087805](https://doi.org/10.1063/5.0087805)

Submitted: 9 February 2022 · Accepted: 20 April 2022 ·

Published Online: 2 May 2022



View Online



Export Citation



CrossMark

Jonathan R. Dietz^{a)} and Evelyn L. Hu

AFFILIATIONS

John A. Paulson School of Engineering and Applied Sciences, Harvard University, Cambridge, Massachusetts 02138, USA

^{a)} Author to whom correspondence should be addressed: jdietz@g.harvard.edu

ABSTRACT

The photoluminescence and spin properties of ensembles of color centers in silicon carbide are enhanced by fabricating optically isolated slab waveguide structures and carefully controlling annealing and cooling conditions. We find that the photoluminescence signal of an ensemble of implanted defects is enhanced in slab waveguides by an order of magnitude over identically implanted bulk defects. The slab waveguide-enhanced photoluminescence of several defect species is used to study recombination and diffusion in the presence of thermal annealing with both rapid quench cooling and a longer return to ambient conditions. The confined mechanical geometry of a thin film is exploited to measure the spin-strain coupling of the negatively charged silicon monovacancy. The methods in this work can be used to exercise greater control on near-surface emitters in silicon carbide and better understand and control the effects of strain on spin measurements of silicon carbide based color centers.

© 2022 Author(s). All article content, except where otherwise noted, is licensed under a Creative Commons Attribution (CC BY) license (<http://creativecommons.org/licenses/by/4.0/>). <https://doi.org/10.1063/5.0087805>

Silicon carbide is a wideband gap semiconductor with many color centers that emit from the visible to the infrared; many of the centers have paramagnetic resonances useful for the construction of quantum memories, single photon sources, magnetometers, and electrometers, to name a few.^{1–5} While both intrinsic and extrinsic color centers benefit from silicon carbide's wealth of manufacturing processes and accessibility as a wafer scale semiconductor platform, numerous challenges remain in realizing high quality device applications. The performance of the color centers is often subject to limitations in brightness and indistinguishability. Beyond issues of extracting light from atomic scale emitters within high index of refraction materials, there are other reasons leading to the relatively low detected photon emission rates of the negatively charged silicon vacancy V_{Si}^- and neutral divacancy $V_{Si}V_C^0$. There is a fast non-radiative decay into the intersystem crossing states of the defect system as compared to its spin conserving radiative decay.⁶ Previous work addresses this by coupling emitters to photonic crystal cavities, resulting in a threefold decrease in the spontaneous emission lifetime and producing an increased luminescence output.⁷ In addition, *charge state conversion* of a defect state can quench an optically bright color center.⁸ Finally, the dipole moment of the center's optical transition may be poorly aligned with its optical excitation. In this study, we demonstrate that slab waveguides alone can significantly enhance the optical and spin properties of surface

ensembles in silicon carbide. We leverage this enhancement to study the recombination of SiC defect centers under different annealing-and-cooling processes, noting the changes in optical and spin signatures of the ensemble.

The formation of SiC defect centers with controlled spatial placement and defect type is critical for their implementation within quantum information systems, strongly depending on the means of defect formation and annealing. Forming centers in a pure, epitaxially grown material requires irradiation with energetic photons, electrons, or ions, which introduce residual damage in the form of interstitials, secondary defects, surface states, and stress.^{9–12} These effects can produce broadened zero phonon lines, spin resonances, and reduced signal to noise in spin readout. Post implantation treatment mitigates some of these effects, recombining unwanted defect species and stabilizing desired defect species.^{13–15} While initial studies have been performed to study the critical temperatures of formation for specific defects, there is need for comprehensive experimental work studying defects' formation, recombination, and diffusion. Fortunately, many of silicon carbide's intrinsic defects have bright optical transitions and spin transitions, useful in studying the relative defect populations and assessing overall material strain. In this work, we study the optical signal of the bright intrinsic defects in silicon carbide: carbon anti-site vacancy ($C_{Si}V_C^{2+}$), silicon monovacancy (V_{Si}^-), and divacancy ($V_{Si}V_C^0$) and the optically

detected magnetic resonance (ODMR) of the k-site V_{Si}^- or V2 line. Starting from the c-axis grown material, we first study the way that the undercut material produces slab waveguide modes that efficiently scatter pump photons into the typically inefficiently excited V1 and V2 lines and the consequent enhancement of the magnetic resonance of the V2 line. Then, using our enhanced ability to identify the constituent defects, we intentionally modify the ensemble, through annealing in air at 600 °C to produce $C_{Si}V_C^{2+}$ and at 850 °C to produce $V_{Si}V_C^0$, followed by either slow cooling or rapid quenching. We monitor the relative population of each defect species after each annealing and cooling process by photoluminescence (PL) measurements and monitor the thin film stress via optically detected magnetic resonance (ODMR) and subsequent focused ion beam (FIB) stress-strain release.

The two samples used in this study were fabricated from epitaxially grown 4H-SiC (Norstel AB). Starting from a bulk, n-type (10^{19} cm^{-3}) wafer of 4H-SiC, layers of p-type (10^{18} cm^{-3}), i-type, and p-type (10^{18} cm^{-3}) materials were epitaxially grown in layer thicknesses of 100, 200, and 100 nm, respectively, to form a p-i-p-n structure. Electron-beam patterning formed patterns of rectangular nanobeam waveguides, approximately 200 nm thick \times 200 nm wide, and 10 μm in length. The nanobeams are suspended through an undercut process that employs a photo-electrochemical (PEC) process, as described in the previous work.^{7,16,17} The PEC process also results in areas of the undercut material that forms 2 μm wide and 200–300 nm thick slab waveguides that extend for distances of 20 μm , the focus of this study. The samples, which are sourced from the same wafer, but represent different fabrication runs, are then bulk implanted at a dose of $1 \times 10^{12} \text{ C}^{12}$ ions and an energy of 70 keV, at 7° off of the c-axis to form an ensemble of color centers. This condition is chosen to create an ensemble of a depth of 132 nm and limited continued penetration into the substrate, as calculated by their stopping range. There will still be some implantation into the substrate; however, we find that the substrate is excessively rough and essentially demonstrates no photoluminescence (see the [supplementary material](#)).

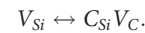
Thermal annealing was carried out on the samples using a quartz tube reactor in air at two temperatures. An initial anneal was performed at 600 °C for 1 h. The goal of this anneal was to allow diffusion of those SiC defects with higher diffusion constants and to form $C_{Si}V_C^{2+}$. A subsequent anneal was carried out at 850 °C for 1 h; these are the conditions that have been reported to form $V_{Si}V_C^{18}$. After each high temperature step, return to room temperature was accomplished either through slow cooling over 6 h or by rapid quenching through immersion in room temperature water.

The PL and V2 ODMR of the ensemble are measured after each thermal annealing and subsequent cooling step. All PL and ODMR measurements are performed in a continuous flow cryostat (Janis ST-500) at 77 K. Excitation (collection) light is delivered (collected) with an NA 0.6 objective and then filtered through a 50 μm pinhole with a measured spot size of 1.0 μm . The PL of $C_{Si}V_C$ and V_{Si} is measured with 300 μW of 632.8 nm from a helium–neon laser. The PL of $V_{Si}V_C$ and k-site V_{Si} centers is measured with 2 mW of 865 nm laser light.

ODMR is measured using a home built confocal ODMR spectrometer equipped with a single photon avalanche detector with 100 μW of 865 nm excitation light and luminescence filtered with 900 nm long-pass and 1000 nm short-pass filters to eliminate the phonon sideband of h-site V_{Si}^- and VV^0 PL. Radio-frequency excitation is supplied from an RF signal generator (Stanford Research System SR384)

and then amplified to 30 dBm (Minicircuits ZHL-2-S+), which is directed to the sample by a closely placed 50 μm wire.

Implantation into SiC can give rise to several defect species; in addition to the V_{Si} , there are V_C 's (carbon vacancies of different charge states), Si and C interstitials, $V_{Si}V_C$ (silicon–carbon divacancies), and Si and C anti-site defects. $C_{Si}V_C$ has an important impact on the number of V_{Si} 's observed, as annealing allows carbon atoms to convert to or from V_{Si} in an equilibrium reaction^{14,15}



To gain insight into this conversion process at different annealing conditions, our data will track the emission of both the V_{Si}^- and the carbon anti-site vacancy pair ($C_{Si}V_C^{2+}$). Carbon anti-site vacancies have two sets of visible zero-phonon lines (ZPLs) corresponding to their inequivalent lattice configurations. ZPLs at 640–670 nm are denoted as A-lines, and ZPLs at 670–680 nm are denoted as B-lines.¹⁹

Figures 1(b) and 1(c) compare the PL of the unannealed defect ensemble in the bulk sample to the PL in the slab waveguide region. Figure 1(b) delineates the spectral region from ~600 to 1100 nm, while Fig. 1(c) delineates the region from 900 to 1300 nm, where we look for V_{Si}^- and possible $V_{Si}V_C^0$ emission. Although there is some indication of $C_{Si}V_C^{2+}$ emission in the bulk material, broad background emission in the slab waveguide, peaking at 700–750 nm, obscures $C_{Si}V_C^{2+}$ emission. Figures 1(b) and 1(c) reveal an order of magnitude higher output intensity for silicon vacancy emission and strong V1 and V2 zero-phonon lines (ZPL). These ZPLs do not appear in bulk spectra, and only V1' appears. We believe that the enhanced luminescence results from the slab waveguide geometry, a result of multiple reflections at the top and bottom surfaces of the slab. In addition, the strong appearance of both V1 and V2 ZPLs in the slab waveguide suggests a larger intermixing of the TM-mode field into the waveguide, enhancing coupling to the V2 transition. V1 and V2 have dipoles aligned nearly orthogonally to the basal plane, coupling poorly to the basal plane-oriented excitation in the bulk. The rough under-surface of the slab waveguide, as shown in scanning electron micrograph images, can result in mixing between the TE character of the laser excitation and the mostly TM character of the V1 and V2 dipole moments.

The ODMR signal of the ensemble is also significantly improved in the undercut material, compared to the bulk. As shown in Fig. 1(d), for measurements taken with no applied magnetic field, the two degenerate spin transitions have broad overlapping 20 MHz linewidths. In the slab waveguide, the magnetic resonance signature is twice as strong as in the bulk material, owing to the enhancement of the V2 dipole transition from slab waveguide confinement. When fitted with a bi-Lorentzian, there is a small splitting of 10 MHz between the normally Kramer-degenerate $|-1/2\rangle \leftrightarrow |-3/2\rangle$ and $|-1/2\rangle \leftrightarrow |-3/2\rangle$ spin subspaces. We attribute this splitting to residual strain in the material that has developed over the course of fabrication and ion implantation.

Thermal annealing of an implanted sample can remove residual unwanted material defects and promote defect recombination. In general, V_{Si} and $C_{Si}V_C$ ZPLs are stronger and better defined in slab samples as compared to bulk samples, so the data shown in Fig. 2 refer to only slab waveguide samples. The improved optical readout of the slab waveguide geometry allows us to monitor defects throughout annealing processes, where defect diffusion and recombination may lower the density and, hence, detectability of the defects. We select two samples from a single fabrication run and show their as-implanted spectra

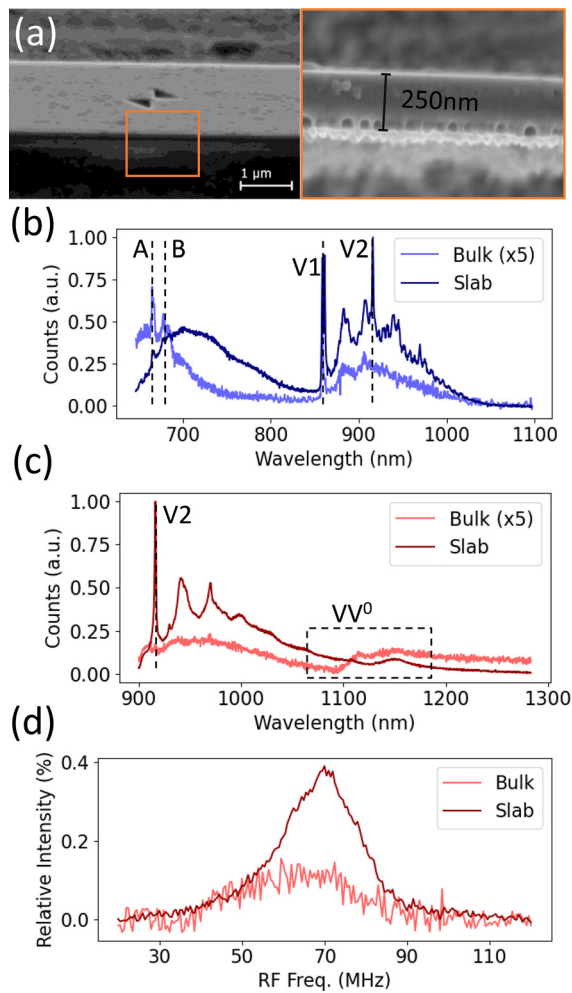


FIG. 1. Slab waveguide enhanced properties of intrinsic defects of silicon carbide. (a) Field-emission scanning electron microscope image of the suspended waveguide structure. Inset: image demonstrating roughened morphology. (b) Photoluminescence of as-implanted intrinsic color centers excited by 632 nm light. (c) Photoluminescence of the k-site V_{Si}^- (V2) center and weak divacancy in bulk and slab waveguides excited by 865 nm light and its (d) corresponding optically detected magnetic resonance.

in Fig. 2 before heat-treatment. Notable is strong defect luminescence at 700 nm present in both samples but that shows up more strongly in the sample corresponding to the data in Figs. 2(b) and 2(d). This variation is common for our samples and appears related to the PEC process used to release the suspended structure. In spite of this variation in defect luminescence, the silicon monovacancy signal in both samples shows very similar intensities.

In Figs. 2(a) and 2(c), the materials are annealed and then allowed to “naturally” return to room temperature. While the 600 °C annealing step increases the V_{Si} fluorescence, further annealing at 850 °C results in a substantially diminished signal. The $C_{Si}V_C$ ZPL emission present in the as-implanted material is no longer discernible after the 600 °C and 850 °C annealing steps masked within the broad 700 nm luminescence peak. This trend, the diminution of the V_{Si} with

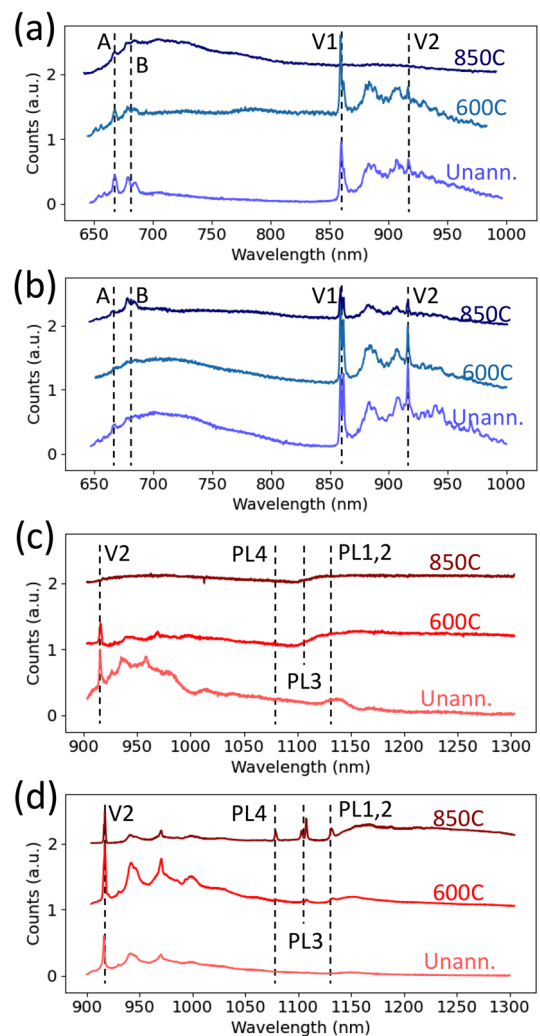


FIG. 2. Evolution of slab ensemble emission over the course of annealing with and without quench cooling. Each temperature condition is offset by 1 arbitrary unit. (a) and (b) Evolution of 632 nm excited carbon anti-site and silicon monovacancy in the case of (a) slow cooling and (b) quench cooling. (c) and (d) Evolution of 865 nm excited silicon monovacancy and divacancy emission in the case of (c) slow cooling and (d) quench cooling. Quench cooling is believed to limit conversion of V_{Si} into $C_{Si}V_C$.

increased annealing temperature, is also observed in the spectrum of Fig. 2(c), where the 850 °C anneal results in an essentially featureless spectrum. Soaking for 5 min in concentrated 47% hydrofluoric acid results only in a slight reduction in the 700 nm peak, suggesting that the loss of desired ensemble emission is more complicated than the presence and influence of surface states (see the [supplementary material](#)).

Figures 2(b) and 2(d) display some dramatically different features when the annealing steps are followed by a “quench cooling” process to return the samples to room temperature. Previous work suggested that the conversion of V_{Si} to $C_{Si}V_C$ through thermal annealing can be limited by rapidly cooling the sample, thus maintaining a relatively

high density of V_{Si} as compared to a sample that is slowly cooled.¹³ Indeed, our results are consistent with those earlier findings.

After quench-cooling from 600 °C, there is a partial reduction of the broad band centered at 700 nm, and no anti-site luminescence appears. The divacancy band is strengthened, and several ZPLs appear. After a further anneal at 850 °C and quench-cooling, the broad band at 700 nm is further suppressed, and the anti-site PL transition is evident. A decrease in V_{Si} is accompanied by an increase in both divacancy and anti-site emissions with the additional appearance of all four VV^0 ZPLs. Finally, the spectrum directly in the vicinity of the V2 line shows minimal background fluorescence, indicating the suppression of PL that would decrease the ODMR signal-to-noise. Importantly, when compared to annealing without quenching, the ZPLs of all three defect species are stable and visible. The quench cooling may constrain the diffusion of the SiC defects and, thus, constrain their recombination or aggregation.

How do the ODMR traces track the various annealing processes? In the case of anneal with slow cooling, the initial 600 °C anneal improves the V2 ODMR signal, as shown in Fig. 3(b), increasing the intensity of the resonance. The linewidth of the transition also narrows slightly, and the strain splitting nearly disappears. There are also satellites to the central ODMR transitions inconsistent with a typical hyperfine interaction, as they are split from the zero field splitting by

three times the strain splitting of the central lines and lack the symmetric structure of hyperfine interactions.²⁰ When annealed further to 850 °C, the ODMR intensity decreases commensurately with the integrated PL [Fig. 2(c)]. Surprisingly, the Lorentzian fitted linewidth of the ODMR continues to decrease, reaching a fitted width of 4.7 MHz. Strikingly, strain splitting redevelops, and the satellite peaks persist, as summarized in Table I. For the quench-cooled samples, 600 °C annealing again results in an ODMR signal with increased intensity; additional satellite lines appear in the ODMR spectrum, and the transition linewidth narrows. The ODMR also indicates a substantially greater amount of the material strain for the quench-cooled samples. After the 850 °C anneal followed by quench-cooling, the splitting in the ODMR is further split, while the linewidth further decreases, dropping to 3.2 MHz, revealing previously unobserved hyperfine lines. Following thermal treatment, residual film strain is assessed by using a focused ion beam (FIB) of gallium ions to release the waveguide structure and then measuring the film deflection via an electron microscope as shown in Fig. 4. We estimate the strain in the released slab using finite element COMSOL simulation and the measured displacement. Using 4H-SiC literature values for silicon carbide's elastic modulus (500 GPa) and Poisson ratio (0.2), we estimate the film strain to be on the order of 0.2%.²¹

The experiments in this paper underscore the important interplay of material geometries and the importance of tracking both luminescence and spin properties of multiple color centers, as various processing conditions are applied. Undercut structures are the basis of optically isolated cavities that can selectively enhance color-center transitions. At a simpler level, the more limited volumes probed (compared to bulk samples), and their visible display of strain, allows us to better track processes of defect formation and recombination. By examining the relative intensity of three bright intrinsic defects, V_{Si} , $C_{Si}V_C$, and $V_{Si}V_C$, in the presence of annealing with or without a subsequent quench-cooling step, it is possible to observe several performance limiting changes. The first is the presence of background luminescence, which is shown to obscure the ZPLs of $C_{Si}V_C$ and also results in poor V2 ODMR contrast. Additionally, it is shown that this undesired emission is enhanced through annealing in air when not rapidly cooled. In contrast, when quench-cooling is employed, undesired emission is suppressed, likely through more limited defect diffusion and recombination during cooling. Finally, our results support a premise that quench-cooling inhibits the recombination of V_{Si} , thus significantly enhancing its emission.

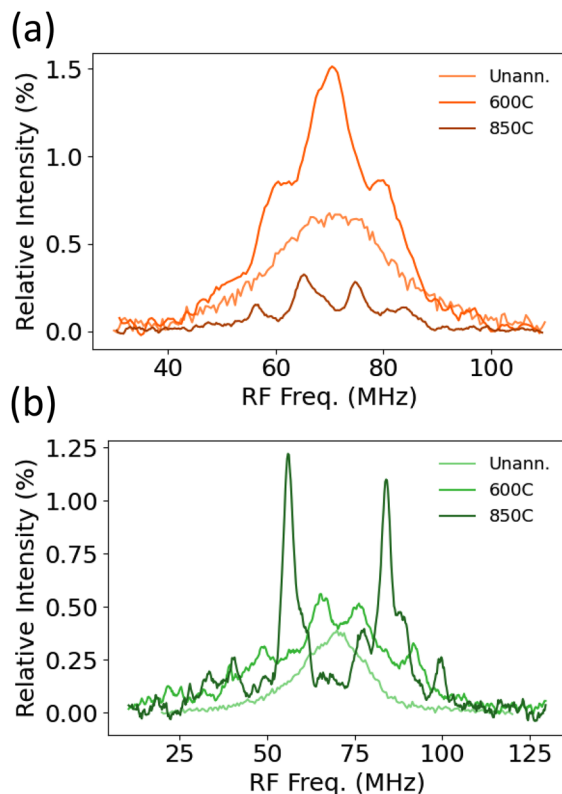


FIG. 3. Evolution of the V2 ODMR spectra (a) without quench cooling and (b) with quench cooling, demonstrating controlled relaxation/enhancement of strain. The longer time allowed in ordinary cooling allows for greater stress release in the sample, compared to the case with quench cooling.

TABLE I. Fitted results of strained ODMR traces shown in Figs. 3(a) and 3(b). Fitting is carried out by fitting a Lorentzian to each of the $\Delta m_s = 1$ transitions subtracting their center frequency to find the splitting and then averaging together their linewidths.

	Quenched		Unquenched	
	Splitting (MHz)	Linewidth (MHz)	Splitting (MHz)	Linewidth (MHz)
Unann.	8.6 ± 0.7	15.4 ± 1.0	10.2 ± 0.6	14.5 ± 1.5
600 °C	11.5 ± 0.2	11.2 ± 0.5	3.2 ± 0.6	8.9 ± 0.7
850 °C	27.6 ± 0.1	3.2 ± 0.2	10.0 ± 0.2	4.7 ± 0.2

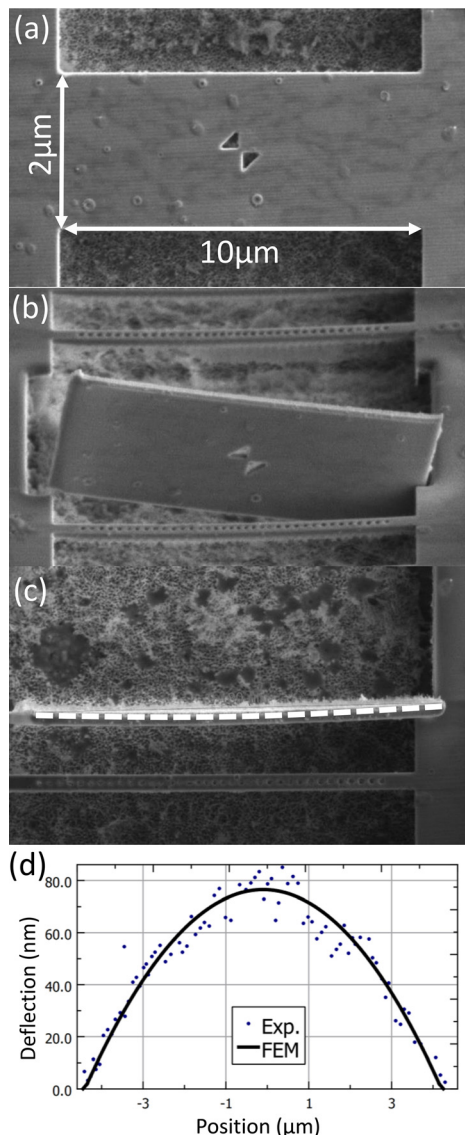


FIG. 4. Direct strain measurement of the waveguide referred to in Figs. 2(b), 2(d), and 3(b) through focused ion beam (FIB) release. (a) Starting from a fully undercut slab waveguide, (b) the waveguide is released by milling the edges with a micromanipulator. (c) Once flipped up, the stress-strain deflection (emphasized by a dotted line) of the released film can be measured directly to (d) infer the quench-cooling mediated stress concentration via finite element model analysis.

The understanding of material strain and its influence on ODMR signatures is critical for control of color centers for device applications, particularly in implanted and near surface emitters. Through careful thermal annealing, it will be possible to mitigate some of these strain effects. Static strain splitting can be either mitigated through careful annealing to release strain or enhanced via rapid cooling. Annealing contributes to significantly narrowed ODMR lines, which can lead to improved sensitivity as a magnetometer or a strain sensor.

Several elements remain to be understood. First and foremost is the identity of the luminescence peaking at 700 nm. This emission band clearly affects the signal to noise of the V_{Si} PL and ODMR contrast in the annealed ensemble. An increase in this emission is clearly associated with quenching of all three of the studied defect species. Second is understanding the intrinsic stress in the SiC starting material. As a $S = 3/2$ defect system, V_{Si} should retain its Kramer's degeneracy under strain, whereas in our work Kramer's degeneracy is clearly lifted (Fig 3) in contrast to theoretical prediction and experiment in 6H-SiC.^{22,23}

Further limiting the volume of the undercut material to smaller dimensions, as applied to nanobeam cavities, with well-controlled annealing conditions may open the way toward defect recombination studies having greater precision.²⁴ Although the surface roughness of undercut structures may introduce unwanted surface states, periodically roughened surfaces may allow us to carry out a better coupling of external laser excitation to match color center dipoles. Finally, careful selection of annealing and thermal quenching conditions yields ensembles with a highly homogeneous strain bias, which could lead to more sensitive quantum sensors.

See the [supplementary material](#) for information regarding implant depth calculations, a detailed cross section of the device geometry, comparison of luminescence from the degenerate n-type substrate and slab waveguide photoluminescence, and impact of hydrofluoric acid pacification of the annealed and slow cooled sample.

J.R.D. acknowledges support from the National Science Foundation via Research Advanced by Interdisciplinary Science and Engineering (RAISE) on Transformational Advances in Quantum Systems (TAQS) Grant No. 1839164-PHY and support from the STC Center for Integrated Quantum Materials under National Science Foundation via Grant No. DMR-1231319. This work was performed in part at the Harvard University Center for Nanoscale Systems (CNS), a member of the National Nanotechnology Coordinated Infrastructure Network (NNCI), which is supported by the National Science Foundation under NSF Electrical, Communications and Cyber Systems Award No. 1541959. The authors would like to further thank Dr. Xingyu Zhang for fabrication support and Aaron Day for assistance with measurements.

AUTHOR DECLARATIONS

Conflict of Interest

The authors have no conflicts to disclose.

DATA AVAILABILITY

The data that support the findings of this study are available from the corresponding author upon reasonable request.

REFERENCES

- R. Nagy, M. Niethammer, M. Widmann, Y.-C. Chen, P. Udvarhelyi, C. Bonato, J. U. Hassan, R. Karhu, I. G. Ivanov, N. T. Son, J. R. Maze, T. Ohshima, Ö. O. Soykal, Á. Gali, S.-Y. Lee, F. Kaiser, and J. Wrachtrup, *Nat. Commun.* **10**, 1954 (2019).
- S. Castelletto, B. C. Johnson, V. Ivády, N. Stavrias, T. Umeda, A. Gali, and T. Ohshima, *Nat. Mater.* **13**, 151 (2014).
- D. Simin, F. Fuchs, H. Kraus, A. Sperlich, P. G. Baranov, G. V. Astakhov, and V. Dyakonov, *Phys. Rev. Appl.* **4**, 014009 (2015).

- ⁴G. Wolfowicz, S. J. Whiteley, and D. D. Awschalom, *Proc. Natl. Acad. Sci. U. S. A.* **115**, 7879 (2018).
- ⁵A. Lohrmann, B. C. Johnson, J. C. McCallum, and S. Castelletto, *Rep. Prog. Phys.* **80**, 034502 (2017).
- ⁶H. B. Banks, Ö. O. Soykal, R. L. Myers-Ward, D. K. Gaskill, T. L. Reinecke, and S. G. Carter, *Phys. Rev. Appl.* **11**, 024013 (2019).
- ⁷D. O. Bracher, X. Zhang, and E. L. Hu, *Proc. Natl. Acad. Sci. U. S. A.* **114**, 4060 (2017).
- ⁸C. F. de las Casas, D. J. Christle, J. Ul Hassan, T. Ohshima, N. T. Son, and D. D. Awschalom, *Appl. Phys. Lett.* **111**, 262403 (2017).
- ⁹A. Hallén, M. S. Janson, A. Y. Kuznetsov, D. Åberg, M. K. Linnarsson, B. G. Svensson, P. O. Persson, F. H. C. Carlsson, L. Storasta, J. P. Bergman, S. G. Sridhara, and Y. Zhang, *Nucl. Instrum. Methods Phys. Res., Sect. B* **186**, 186 (2002).
- ¹⁰C. Kasper, D. Klenkert, Z. Shang, D. Simin, A. Gottscholl, A. Sperlich, H. Kraus, C. Schneider, S. Zhou, M. Trupke, W. Kada, T. Ohshima, V. Dyakonov, and G. V. Astakhov, *Phys. Rev. Appl.* **13**, 044054 (2020).
- ¹¹S. Castelletto, A. F. M. Almutairi, K. Kumagai, T. Katkus, Y. Hayasaki, B. C. Johnson, and S. Juodkasis, *Opt. Lett.* **43**, 6077 (2018).
- ¹²H. Kraus, D. Simin, C. Kasper, Y. Suda, S. Kawabata, W. Kada, T. Honda, Y. Hijikata, T. Ohshima, V. Dyakonov, and G. V. Astakhov, *Nano Lett.* **17**, 2865 (2017).
- ¹³J. B. S. Abraham, C. Gutsell, D. Todorovski, S. Sperling, J. E. Epstein, B. S. Tien-Street, T. M. Sweeney, J. J. Wathen, E. A. Pogue, P. G. Brereton, T. M. McQueen, W. Frey, B. D. Clader, and R. Osiander, *Phys. Rev. Appl.* **15**, 064022 (2021).
- ¹⁴X. Wang, M. Zhao, H. Bu, H. Zhang, X. He, and A. Wang, *J. Appl. Phys.* **114**, 194305 (2013).
- ¹⁵R. Kuate Defo, X. Zhang, D. Bracher, G. Kim, E. Hu, and E. Kaxiras, *Phys. Rev. B* **98**, 104103 (2018).
- ¹⁶D. O. Bracher and E. L. Hu, *Nano Lett.* **15**, 6202 (2015).
- ¹⁷A. P. Magyar, D. Bracher, J. C. Lee, I. Aharonovich, and E. L. Hu, *Appl. Phys. Lett.* **104**, 051109 (2014).
- ¹⁸N. T. Son, P. Carlsson, J. ul Hassan, E. Janzén, T. Umeda, J. Isoya, A. Gali, M. Bockstedte, N. Morishita, T. Ohshima, and H. Itoh, *Phys. Rev. Lett.* **96**, 055501 (2006).
- ¹⁹J. W. Steeds, *Phys. Rev. B* **80**, 245202 (2009).
- ²⁰N. T. Son, P. Stenberg, V. Jokubavicius, T. Ohshima, J. U. Hassan, and I. G. Ivanov, *J. Phys.: Condens. Matter* **31**, 195501 (2019).
- ²¹J. Chen, A. Fahim, J. C. Suhling, and R. C. Jaeger, in *18th IEEE Intersociety Conference on Thermal and Thermomechanical Phenomena in Electronic Systems (ITherm)* (IEEE, 2019), pp. 835–840.
- ²²I. D. Breev, A. V. Poshakinskiy, V. V. Yakovleva, S. S. Nagalyuk, E. N. Mokhov, R. Hübner, G. V. Astakhov, P. G. Baranov, and A. N. Anisimov, *Appl. Phys. Lett.* **118**, 084003 (2021).
- ²³Ö. O. Soykal and T. L. Reinecke, *Phys. Rev. B* **95**, 081405 (2017).
- ²⁴M. N. Gadalla, A. S. Greenspon, R. K. Defo, X. Zhang, and E. L. Hu, *Proc. Natl. Acad. Sci.* **118**, e2021768118 (2021).